

Gradients of Stellar Population Properties and Evolution Clues in a Nearby Galaxy M 101

Lin Lin ^{1,2}, Hu Zou ³, Xu Kong ^{1,2}, Xuanbin Lin ^{1,2}, Yewei Mao ^{1,2}, Fuzhen Cheng ^{1,2},
Zhaoji Jiang ³, Xu Zhou ³

ABSTRACT

Multi-band photometric images from ultraviolet and optical to infrared are collected to derive spatially resolved properties of a nearby Scd type galaxy M 101. With evolutionary stellar population synthesis models, two-dimensional distributions and radial profiles of age, metallicity, dust attenuation, and star formation timescale in the form of the Sandage star formation history are obtained. When fitting with the models, we use the $IRX-A_{FUV}$ relation, found to depend on a second parameter of birth rate b (ratio of present and past-averaged star formation rate), to constrain the dust attenuation. There are obvious parameter gradients in the disk of M101, which supports the theory of an “inside-out” disk growth scenario. Two distinct disc regions with different gradients of age and color are discovered, similar to another late-type galaxy NGC 628. The metallicity gradient of the stellar content is flatter than that of H II regions. The stellar disk is optically thicker inside than outside and the global dust attenuation of this galaxy is lower, compared with galaxies of similar and earlier morphological type. We highlight that a variational star formation timescale describes the real star formation history of a galaxy. The timescale increases steadily from the center to the outskirt. We also confirm that the bulge in this galaxy is a disk-like pseudobulge, whose evolution is likely to be induced by some secular processes of the small bar with relatively young age, rich metal, and much dust.

Subject headings: Galaxies: individual(M 101) — Galaxies: evolution — Galaxies: photometry — Galaxies: bulge

¹Center for Astrophysics, University of Science and Technology of China, Hefei 230026, China; linlin@mail.ustc.edu.cn, zouhu@nao.cas.cn, xkong@ustc.edu.cn

²Key Laboratory for Research in Galaxies and Cosmology, Chinese Academy of Sciences, Hefei 230026, China

³National Astronomical Observatories, Chinese Academy of Sciences, Beijing 100012, China

1. INTRODUCTION

Galaxy formation and evolution are complicated matters which have not yet come to a complete and coherent understanding. In the cosmological Λ cold dark matter (Λ CDM) model, galaxies are formed by collapsing and cooling of gas. Galaxies gain in mass and determine their shape and structure through clustering and merging. This model has been very successful at reproducing observations in the formation of massive galaxies at high redshift (Daddi et al. 2005; Trujillo et al. 2006). In recent years, however, the role of secular evolution on nearby galaxies has been found to be more and more significant, compared with the violent merging and clustering in the early universe (Kormendy & Kennicutt 2004; Carollo et al. 2007; Fisher & Drory 2010; Kormendy et al. 2010). A lot of observational evidence shows that evolutions of bulge and disk are being leaded by some secular processes, which are caused by the asymmetric gravitational potential from oval, bar, or spiral structure (Kormendy & Kennicutt 2004).

For a galaxy, a variety of processes might act during its formation and evolution, such as merging, satellite accreting, star forming, and radial migrating (Wyse et al. 2006; Roškar et al. 2008). The consequent long-time star formation and chemical enrichment would lead to non-homogeneous stellar population properties (e.g., age and metallicity). In general, nearby elliptical and spiral galaxies are bluer outwards (Peletier et al. 1990; Tamura & Ohta 2003), dwarfs show redder outskirts (Cameron et al. 2009), and the disks of majority of spiral galaxies have radial abundance gradients.

Spectral line indices (Lick system) are effective tracers of stellar populations for early-type galaxies (Worthey 1994). But for late-type galaxies, it is difficult to obtain reliable measurements due to low surface brightness and contaminated stellar continua by gaseous emission lines of star-forming regions. Thus, many published studies focus on gradients of stellar population properties derived by the emission lines. Zaritsky et al. (1994) and van Zee et al. (1998) found H II regions to have an average metallicity gradient of $-0.05 \text{ dex kpc}^{-1}$. Recent deep investigations with absorption-line spectra have highlighted the presence of non-monotonic colors and stellar population gradients in spiral galaxies (MacArthur et al. 2004; Bakos et al. 2008; MacArthur et al. 2009; Sánchez-Blázquez et al. 2009). However, gradients measured by different authors have large discrepancies, because it is difficult to disentangle the effects of age, metallicity, and dust extinction.

Multi-wavelength photometric data can help us to break this kind of degeneracy. Observed stellar light is emitted by stars in galaxies and might be reprocessed by gas and dust in the surrounding interstellar medium. So UV-to-IR spectral energy distributions (SEDs) contain a large amount of information about galaxies, such as the stellar population, stellar mass to light ratio, and behaviors of the gas and dust contents. We have analyzed spatially

resolved stellar population properties for two nearby galaxies using different evolutionary population synthesis (EPS) models (Kong et al. 2000; Li et al. 2004; Zou 2011a; Zou et al. 2011c). In these papers, optical or UV-to-IR SED for each part of galaxies was extracted from multi-band photometric images so as to obtain various parameters by fitting with models. Our purpose is to investigate the nature and connection of disks and bulges, analyze detailed stellar population properties, and get hints on the star formation history and galactic evolution.

In this paper, we present a two-dimensional analysis of a nearby galaxy M 101. M 101 (NGC 5457, $\alpha = 14^{\text{h}}03^{\text{m}}12.5^{\text{s}}$, $\delta = +54^{\circ}20'56''$) is a face-on Scd galaxy at a distance of 7.4 Mpc. It has an apparent scale of about 36 pc per arcsec, which provides an excellent opportunity for anatomizing underlying stellar populations. The paper is structured as follows. Section 2 briefly describes optical photometric observations, archival data in other bands, and corresponding data reduction. Section 3 explains the way to construct model SEDs. In Section 4, we detailedly introduce the technique to constrain dust attenuation so as to degrade the degeneracy among different parameters. The fitting method and its reliability are provided in Section 5. The distributions and radial profiles of different parameters are shown in Section 6. At last, Sections 7 and 8 respectively give some discussions and conclusions. We use the major-axis position angle of 39° and inclination angle of 18° (Bosma et al. 1981) to deproject the galaxy throughout our paper.

2. OBSERVATIONS AND DATA REDUCTION

2.1. Optical Intermediate-band Observations

M 101, as one of galaxies in the Beijing-Arizona-Taiwan-Connecticut (BATC) survey, was observed by the 60/90 cm Schmidt telescope at the Xinglong Station of National Astronomical Observatories of China (NAOC). A 2048×2048 CCD is mounted at the focal plane of the telescope. The field of view (FOV) is about $58' \times 58'$ and the pixel scale of the CCD is about $1.7''$. The BATC photometric system includes 15 intermediate-band filters with bandwidths of about 200–300 Å, covering the wavelength range of 3300 – 10000 Å. These filters are designed to avoid the contamination from night sky emission lines (Fan et al. 1996). Multiple exposures for each band were taken from 1995 November to 2004 February. Table 1 lists the effective wavelengths of those filters and some statistics of the stacked images.

All observed images are treated by the data processing procedures customized for the BATC survey as described in the paper of (Fan et al. 1996). The pipelines include several

steps as following: a) overscan correction; b) subtractions of bias and dark current; c) flat-field correction; d) image stacking of multiple exposures, where bad pixels and cosmic rays are removed; e) astrometry by the UCAC3 (USNO CCD Astrograph Catalog) catalogue; f) flux calibrations of the stacked images by standard stars observed at photometric nights (for full knowledge of the calibration, refer to the paper of Zou et al. (2011c)). Finally, the CCD digital counts in ADU are converted to flux density in $\text{erg s}^{-1}\text{cm}^{-2}\text{Hz}^{-1}$.

2.2. Archival Data in Other Bands

GALEX & XMM-OM ultraviolet images GALEX imaging observations are centered at 1529 Å and 2312 Å for the far-ultraviolet (FUV, 1350–1750 Å) and near-ultraviolet (NUV, 1750–2750 Å) bands, respectively (Martin et al. 2005). M 101 was observed in 2008 April and May as part of the public Guest Investigator (GI) program, with exposure times of 13294 s for FUV and 13293 s for NUV. The PSF FWHMs of the images are $\sim 4.2''$ and $\sim 4.6''$, and sensitivity limits (1σ) for these two bands are 2.04×10^{-19} and 1.03×10^{-19} $\text{erg s}^{-1}\text{cm}^{-2}\text{Å}^{-1}$ per pixel. More details about the GALEX data are given in Bianchi et al. (2005).

The XMM Optical Monitor (XMM-OM) also observed this galaxy in six broad bands: VUW1, UVM2, UVW2, U , B , and V (Kuntz et al. 2008). The central wavelengths are 2120 Å, 2310 Å, 2910 Å, 3440 Å, 4500 Å, and 5430 Å, respectively. Considering the signal-to-noise ratio (S/N), we only use the UVW1 and U band images to reinforce the observation data in the NUV wavelength region. The total exposure times of these two bands are 2317 s and 927 s, which yield 1σ sensitivity limits of 1.15×10^{-30} and 1.89×10^{-30} $\text{erg s}^{-1}\text{cm}^{-2}\text{Hz}^{-1}$ per pixel. Note that a small part (west) of M 101 was not covered in the U band.

2MASS near-infrared images Near-infrared (NIR) images of M 101 in the J , H , and K_s bands (1.2, 1.65, and 2.2 μm , respectively) are obtained from the 2MASS Large Galaxy Atlas (Jarrett et al. 2003). The FWHMs of the mosaics are estimated to be about $2.5''$ and the sensitivity limits (1σ) are 3.29×10^{-29} , 5.59×10^{-29} , and 5.89×10^{-29} $\text{erg s}^{-1}\text{cm}^{-2}\text{Hz}^{-1}$ per pixel.

Spitzer infrared images As part of the Local Volume Legacy Survey (Lee et al. 2008; Kennicutt et al. 2007), M 101 was observed in 2004 April by both the Infrared Array Camera (IRAC; 3.6, 4.5, 5.8, and 8.0 μm) and the Multi-Band Imaging Photometer (MIPS; 24, 70, and 160 μm). Four IRAC mosaics provide a view of the old stellar population and/or

emission from polycyclic aromatic hydrocarbons (PAHs). The FWHM of each mosaic is about $2''$ and the sensitivity limits at 1σ are 2.72×10^{-30} , 3.47×10^{-30} , 1.36×10^{-29} , and 1.24×10^{-29} erg s $^{-1}$ cm $^{-2}$ Hz $^{-1}$ per pixel. Three MIPS bands trace thermal radiations from the warm and cool dust. The MIPS mosaics have measured FWHMs of about $6.0''$, $18''$, and $40''$. Sensitivity limits at 1σ are 2.35×10^{-29} , 1.84×10^{-27} , and 8.74×10^{-27} erg s $^{-1}$ cm $^{-2}$ Hz $^{-1}$ per pixel.

2.3. Image Preprocessing Before Extracting the SED

In order to investigate the physical properties of M 101 in a spatially resolved manner, we plan to extract the SED pixel-by-pixel. As the images come from different telescopes and were taken under different observational conditions, some steps of image preprocessing (similar to Zou et al. (2011c)) are required: pixel scaling, masking stars, removing the sky background, convolution of the PSFs, and smoothing.

Pixel scaling As the images in various bands have different spatial resolutions, we adjust these images to the same pixel scale and direction as the BATC images ($1.7''$ per pixel, north is up and east at the left). The pixel scale of $1.7''$ corresponds to about 61 pc at the distance of M 101.

Masking stars Foreground bright field stars are masked according to the 2MASS Point Source Catalog (Skrutskie et al. 2006) and the corresponding areas are filled with the values of their nearest pixels.

Sky background subtraction Source signals are firstly identified by SExtractor (Bertin & Arnouts 1996) and masked, then the sky background maps are obtained by the polynomial fitting method with remaining background pixels.

PSF convolution The PSF for each band is calculated by the PSFEx software¹ (Bertin 2011). All the images are convolved to the FWHM of $6''$ in $24 \mu\text{m}$ by the PSFMATCH task in IRAF².

¹<http://www.astromatic.net/software/psfex>

²<http://iraf.noao.edu/>

Image smoothing To improve the S/N for galactic outskirts, a boxcar averaging method, as shown in Kong et al. (2000) and Zou et al. (2011c), is performed on all images. Here, the smoothing window size depends on the S/N of the BATC *i*-band image and the photometric error for each pixel in the specified band is estimated with the S/N.

Figure 1 displays the processed GALEX, BATC, 2MASS, and Spitzer images of M 101. The morphology of this galaxy belongs to the typical late-type spiral galaxy. Star-forming spiral arms dominate the galaxy morphology at UV bands. Most of the UV-bright knots coincide with giant H II regions. The *J*, *H*, and *K_s* images only show features of the bulge and bright inner disk due to short exposures. The Spitzer 3.6 and 4.5 μm trace the stellar mass and other three bands are filled with dust radiation in addition to stellar light. The SED for each pixel is extracted and will be fitted with models as explained later. These SEDs are corrected by the foreground Galactic extinction, which is 0.009 mag in $E(B - V)$ (Schlegel et al. 1998).

3. CONSTRUCTION OF SED MODELS

Stellar population synthesis fitting, including both the model prediction and fitting procedure, has been improved significantly in the past few decades (Tinsley 1972; Silva et al. 1998; Vazdekis 1999; Bruzual & Charlot 2003; Salim et al. 2007; Groves et al. 2008; Noll et al. 2009). This technique can be used to effectively derive a series of physical properties of galaxies, such as redshift, stellar mass, star formation rate (SFR), dust mass, and metallicity (da Cunha et al. 2008; Zibetti et al. 2009; Kennicutt et al. 2009; Zou et al. 2011b,c). In the following contents, we will describe some aspects of the evolutionary stellar population synthesis and create a library of SED models.

The population synthesis code of Bruzual & Charlot (2003), hereafter BC03, is used to generate evolutionary stellar population synthesis models. We adopt the IMF of Chabrier (2003) with lower and upper mass limits of $0.1 M_{\odot}$ and $100 M_{\odot}$. The Chabrier IMF is preferred over the Kroupa (Kroupa 2002) and Salpeter (Salpeter 1955) IMFs because of its better agreement with the number counts of brown dwarfs in the galactic disk (MacArthur et al. 2004). Recycling is not considered and the ejected gas is reused in the new star formation episodes.

We choose the “delayed-exponential” star formation history (SFH) from the BC03 code. This kind of SFH (“Sandage-like” SFH; hereafter Sandage SFH) can describe the increased SFR and is thought to be more realistic (Gavazzi et al. 2002). It can be expressed as

$$\Psi(t) = \tau^{-2} t \exp(-t/\tau) ,$$

where t is the age, τ is the star formation timescale, and $\Psi(t)$ is the SFR, whose maximum is located at $t = \tau$. Compared with the simple exponentially declining SFH, the Sandage SFH is characterized by a delayed rise in the SFR followed by an exponential decline. The decline rate is determined by the value of τ . MacArthur et al. (2004) showed that the two model grids are quite similar in the color-color space, but the Sandage SFH gives a younger average age ($\sim 0.5\text{--}2$ Gyr) and slightly higher metallicity for a given color.

To denote the star formation activity, we use the b parameter depicted in Scalo & Struck-Marcell (1986). It is expressed in terms of the ratio of the present to past-averaged star formation rate as

$$b = \frac{\psi(t_0)}{\bar{\psi}} = \frac{t_0 \psi(t_0)}{\int_0^{t_0} \psi(t) dt},$$

where t_0 is the current age and $\psi(t_0)$ is the SFR at t_0 .

With the above SFH and BC03 code, we create a library of stochastic models ($\sim 10^5$) following the method of Kauffmann et al. (2003). We take the age to be uniformly distributed over the interval between 1 Myr to 13.5 Gyr. The star formation timescale τ is distributed according to the probability density function of $p(\gamma = 1/\tau) = 1 - \tanh(8\gamma - 6)$ (da Cunha et al. 2008) in order to avoid oversampling EPS models with short τ , where γ is uniformly sampled over the interval of 0–1. Metallicity is set to be uniformly distributed in the range of $0.02\text{--}2 Z_\odot$.

4. CONSTRAINT OF THE DUST ATTENUATION

Interstellar dust affects appearances of a galaxy in different bands. It absorbs and scatters short-wavelength stellar light and reradiates in infrared, making objects appear dimmer and redder. During fitting the observed SED with models, we need to consider the dust attenuation. Since there have been three free parameters (age, metallicity, and star formation timescale) in the models already, we try to seek a feasible method to constrain the dust extinction so as to degrade the degeneracy effect among fitted parameters.

Based on the assumption of an energy balance, i.e., a fraction of UV photons are absorbed by dust and then the energy is completely reemitted in middle IR and FIR, the combination of the IR luminosity and rest UV luminosity might be the most reliable way to estimate the dust attenuation (Buat 1992; Meurer et al. 1999). Although almost independent on the geometry of dust and extinction law, the ratio of the total IR (TIR) and FUV luminosity (so-called IRX in the form of $\log(L_{\text{TIR}}/L_{\text{FUV}})$) used as an estimator of the dust attenuation, is found to depend on the age of underlying stellar population.

For star forming regions, the IRX- A_{FUV} relation shows an overall consistency within $\pm 1\sigma$ uncertainty (Hao et al. 2011). However, for more evolved stellar populations, FIR emission origins from both high-energy photons (mainly UV photons) and optical photons of intermediate-age stars, which are both reradiated by dust. Hence, the IRX- A_{FUV} relation might not be suitable for low-SFR populations or quiescent populations (Kong et al. 2004; Cortese et al. 2008; Mao et al. 2012).

With our spectral library established in the previous section, we investigate the dependence of IRX- A_{FUV} relation on different parameters. Each synthetic model in the library is reddened by the extinction law of Fitzpatrick (1986). The coefficients in the parameterized function come from Rosa & Benvenuti (1994), which is adapt to M 101. This extinction law is similar to the Galactic law except for a much weaker 2175 Å bump. The extinction A_{FUV} is sampled in the range of 0 – 8 mag. For normal star-forming galaxies, the typical range of A_{FUV} is 0 – 4 mag.

Figure 2 displays the relation between IRX and A_{FUV} within different parameter intervals. The TIR flux in IRX is calculated as the energy difference between the original dust-free model spectrum and corresponding reddened spectrum. The FUV flux is computed by convolving the reddened spectrum with the transmission curve of the GALEX FUV filter. The IRX- A_{FUV} relation calibrated by Hao et al. (2011) is overplotted in solid lines. From this figure, we can conclude that for older stellar populations ($t > 5$ Gyr), shorter star formation timescales ($\gamma > 0.6$ Gyr $^{-1}$), or lower birth rates ($b < 0.5$), the IRX- A_{FUV} correlation becomes looser and the dust attenuation might be overestimated if just considering a simple relation derived from star forming regions. We also notice that the relation seems not change with metallicity.

To find a proper second parameter that affects the IRX- A_{FUV} relation, we introduce the formula as presented in Hao et al. (2011):

$$A_{\text{FUV}} = 2.5 \log(1 + \alpha \times 10^{\text{IRX}}), \quad (1)$$

where α is a scale factor. The larger the value of α is, the steeper the relation curve becomes.

For each model spectrum, we calculate the α value by using Equation (1). Figure 3 shows the scale factor α as functions of age, metallicity, star formation timescale, and birth rate. A very tight relation between α and b can be seen. The scale factor increases monotonically with the birth rate, that is, the IRX- A_{FUV} relation strongly depends on the birth rate. We fit the α - b relation with a seven-order polynomial, shown as below:

$$\alpha = 0.0377 + 2.8669b - 8.6302b^2 + 15.3222b^3 - 15.6703b^4 + 9.0869b^5 - 2.7713b^6 + 0.3451b^7. \quad (2)$$

Actually, for normal star-forming galaxies, α is about 0.46 (Hao et al. 2011). For

starburst galaxies with larger star birth rates, α is about 0.6 (Meurer et al. 1999).

5. FITTING METHOD AND RELIABILITY TESTING

5.1. Chi Square Minimization

Model spectra are convolved with the transmission curves of the UV, optical, and near infrared (3.6 and 4.5 μm) bands to generate a set of model SEDs. A simple χ^2 minimization of the differences between model SEDs and observed SEDs is used to derive the optimal values of parameters (for the convolution and minimization methods, refer to the papers of Kong et al. (2000) and Zou et al. (2011c)).

For a given observed SED, the χ^2 value is computed for each model and the optimal parameter estimates are calculated by the probability distribution function $p = \exp(-\chi^2/2)$ (Kauffmann et al. 2003; Salim et al. 2007). The expectation value of a parameter x can be expressed as

$$\bar{x} = \frac{\sum p_i x_i}{\sum p_i},$$

and the standard deviation is

$$\sigma_x = \sqrt{\frac{\sum p_i (x_i - \bar{x})^2}{\sum p_i}},$$

where x represents t , τ , or Z .

While fitting with the models, we use the constraints of Equation (1) and (2) to tie the dust attenuation A_{FUV} to IRX and the birth rate b of the stellar population. Here, b is to be determined. The value of IRX is calculated according to its definition, where

$$L(\text{FUV}) = \nu L_\nu(\text{FUV}),$$

and $L(\text{TIR})$ is calculated with the 8 μm and 24 μm luminosities (Calzetti et al. 2005):

$$\log L(\text{TIR}) = \log L(24\mu\text{m}) + 0.908 + 0.793 \log \frac{L_\nu(8\mu\text{m})}{L_\nu(24\mu\text{m})}.$$

The 8 μm flux is dominated by both the dust radiation and stellar continuum, so the 8 μm luminosity is estimated according to the recipe of Pahre et al. (2004).

In the rest of this paper, we convert the extinction value of A_{FUV} to A_V with the M101 extinction law in order to compare the results with other measurements in literatures, where $A_{\text{FUV}} = 2.67 A_V$.

Figure 4 demonstrates the observed SEDs and best fitted models at different galactocentric radii. In this figure, we can see that the models fit the observed SEDs very well except for the FUV band due to lack of extreme horizontal-branch stars in the stellar population models (Ma et al. 2009). The upper panel of this figure presents that the center of M101 is younger, more metal-rich, and more dusty. The circumnuclear region as shown in the middle panel contains classical old bulge-like stellar populations and the outer region of the disk in the bottom panel is relatively younger.

5.2. Reliability of the Fitting Method

In order to check the reliability of our fitting method, we create a series of artificial SED libraries for testing. Firstly, about 1000 SEDs are generated with random values of age, metallicity, star formation timescale, and extinction, which is the same process as in Section 3. Secondly, for a given S/N in the BATC h band, we find the corresponding average h -band magnitude from the observed magnitude-error diagram of M 101, where the error $\sigma = 2.5\log_{10}(1 + 1/R)$, R is the S/N. All the artificial model SEDs are scaled to this h -band magnitude. Thirdly, a gaussian noise with the standard deviation of σ is added to the scaled magnitude in each band.

Figure 5 shows the capability of reproducing parameters by the fitting method. The simulated SED library used for testing has a photometric S/N of 10. The resulted RMSs for age t in logarithm, metallicity ($\log Z$), birth rate b , and extinction A_V are about 0.13 dex, 0.10 dex, 0.19, and 0.07 mag, respectively. Another free parameter τ , not drawn in this figure, shows a much larger scatter due to its relatively weak insensitivity to SEDs. Table 2 gives parameter uncertainties estimated after fitting the simulated SEDs with different S/Ns.

6. TWO DIMENSIONAL DISTRIBUTIONS OF DIFFERENT PARAMETERS

In this section, we will show the distributions of age, metallicity, dust extinction, and the star formation timescale of M 101 derived by the stellar population synthesis model fitting. The deprojected radial profiles of different parameters only relate to the regions without the effect of H II regions.

6.1. IRX and Extinction Maps

Figure 6 shows the IRX and A_V maps and their own radial profiles. Both the IRX and A_V maps present spiral arm-like structures and obvious radial gradients. The average extinction decreases from about 0.4 mag in the inner disk to about 0.05 mag at the galactic edge. Thus, the stellar disk of M 101 is optically thicker in the inside than in the outside. The central region of M 101 seems to be dusty, whose average extinction is about 0.41 mag. The global extinction of the whole galaxy is about 0.24 mag, implying the optically thin interstellar medium, which is also indicated in the paper of Boissier et al. (2004). Some statistical studies show that the average extinction of Sc–Sd type galaxies is about 0.32 mag, lower than that of Sa–Sb type galaxies (0.48 mag) (Boselli et al. 2003; Muñoz-Mateos et al. 2009). In addition, from the radial profiles in Figure 6, we notice that IRX has its maximum value in the bulge (the effective radius is about 12 arcsec (Fisher et al. 2009)) and inner disc regions, where A_V shows its minimum. It should be reasonable, because in the bulge and inner disk, a considerable fraction of the TIR flux is contributed by old stellar populations.

To check the reliability of our extinction determination, we present the extinction measurements of H II regions derived by the Balmer decrement in Figure 7. Here, filled circles in this figure are nebular extinctions calculated with spectra of the Multiple Mirror Telescope (MMT). These spectra were obtained in 2012 February under the support of the Telescope Access Program (TAP). For detailed information about the observation and data reduction of MMT spectra, we will publish a paper in the near future (Lin et al. 2013; in preparation). Other extinction values in the figure come from McCall et al. (1985), Kennicutt & Garnett (1996), and Bresolin (2007), where $A_{H\alpha}$ is converted to A_V by using the M 101 extinction law. There is a rough gradient (although somewhat diffuse) in the extinction distribution of H II regions. Nebular extinctions are larger than the stellar extinctions and an empirical relationship was derived by Calzetti (2001): $A_V^{\text{star}} = 0.44A_V^{\text{neb}}$.

In Figure 8, we compare the stellar extinctions derived in this paper with those from nebular emission lines. The spectra of H II regions were obtained by long-slit or fiber spectrographs with apertures ranging from 2'' to 10''. Stellar extinctions in this figure are determined as median values within 6'' apertures at the same positions of those H II regions. The solid line in this figure shows a least-squares fit to the data points, yielding $A_V^{\text{star}} = 0.32(\pm 0.01)A_V^{\text{neb}} + 0.06(\pm 0.01)$. The Pearson correlation coefficient is 0.62. It is slightly flatter than that of Calzetti (2001), partly because the PSF convolution and image smoothing might smooth the stellar extinction.

In this paper, we simply assume a foreground screen of uniform dust and the extinction law is same overall the galaxy. But by calculating the radiative transfer models, Pierini et al.

(2004) discovered that there might be some different behaviors of the attenuation function in the galaxy bulge and disk. In general, the average slope of the extinction law increases with the opacity. A homogeneous dust distribution would produce a little larger attenuation than a clumpy one.

6.2. Metallicity Map and the Radial Gradient

The metallicity map in Figure 9 shows that there are a number of knots with high metallicities associated with the spiral arms. The dusty core is found to be more metal-rich than the surrounding environment. The abundance in the inter-arm regions is relatively poor. The average metallicity of the whole galaxy is close to half of the solar abundance.

From the radial profile in Figure 9, there is a relatively shallow decreasing gradient, which is about -0.011 ± 0.006 dex kpc^{-1} . Gas-phase abundances of H II regions in M 101 have been measured by many authors (Kennicutt & Garnett 1996; Kennicutt et al. 2003; Bresolin 2007). Oxygen abundances are derived by using different methods based on strong lines or auroral lines. We plot the collected Oxygen abundances from the literatures along the galactocentric distance in Figure 10. The metallicity measurements from the MMT spectra as described previously are also shown in this figure. We find an average gradient of about -0.045 dex kpc^{-1} , which is equal to the $[\text{Fe}/\text{H}]$ gradient if assuming the same chemical composition as the Sun (Grevesse & Sauval 1998). In contrast, the abundance gradient of the circumambient stellar content is much flatter than that of H II regions.

6.3. Age in Different Components

Figure 11 shows the age distribution of M 101 in two dimensions and its radial profile. The stellar population in the central region is older, while it is younger in outer regions. The oldest part appears in the inner disk (around the galactocentric distance of ~ 20 arcsec). Spiral arms, where many H II regions are located, are much younger than other components. The inter-arm areas are filled with relatively older stellar populations.

It is worthwhile to mention that the bulge has a stellar age that is younger than the surrounding inner disk. This kind of young bulge is also found in several late-type disk galaxies (Carollo et al. 2007). Similar results were reported by Ganda et al. (2007) based on their IFS (Integrated Field Spectroscopy) observations in the central regions of late-type galaxies.

We also notice in the radial age profile that there are two distinct components in the

disk. The inner disk, ranging from 0.3 to 1.0 arcmin, is dominated by intermediate age populations. However, the age gradient in outer disk ($R > 1.0$ arcmin) is quite flat. This kind of two parts in the disk with distinct age gradients is also found in the studies of resolved stellar populations of M33 and NGC 628 (Williams et al. 2009; Zou et al. 2011c).

Colors tracing the age are plotted in Figure 12 in order to compare with the age characteristics. The FUV–NUV color reveals the same trend as the age profile. As also shown in Bianchi et al. (2005), there is a gradient of this color in M 101, implying younger stellar populations in the outer disk regions. Another age-sensitive index is the BATC $b - c$ color, which approximates the index of D4000 (4000 Å break). Both colors indicate that the bulge is somewhat younger and two distinct parts in the disk presenting different color gradients: steeper inside and flatter outside.

6.4. Star Formation Timescale

Figure 13 shows the map of star formation timescale and its radial profile. We can see that the timescale increases steadily from the center to the outskirts. It is shorter in the bulge and longer in the disk, that is, the star forming in the inner part of M 101 is extinguished and that in the outskirts might be continuous. The average star formation timescale of the bulge, inner disk, and outer disk is about 1.1, 1.2, and 1.6 Gyr ($60 < R < 400$ arcsec), respectively. The average timescale of some H II regions in the outer disk may reach about 2.6 Gyr.

7. DISCUSSION

7.1. Gradients

Radial surface brightness and color are the most direct observational quantities to investigate the properties of stellar populations and the evolution status in nearby galaxies, but it is difficult to relieve the degeneracy effect. Using synthetic spectral models and UV-to-IR panchromatic photometric SEDs, we have distinguished the effects of age, metallicity, and dust extinction.

The radial age profile of M 101 as shown in Section 6.3 presents a comparatively younger bulge (see the discussion in next section), an older inner region of the disk with a steeper age gradient, and a younger outer disk region with a flatter gradient. Two distinct disc components might be caused by differential rotations and a nonaxisymmetric self-gravitating

mode of spiral arms, which make the inner disk contract and the outer region stretch (Zou et al. 2011c). Certainly, events, such as gas accretion and interacting with another galaxy, also trigger star formation in the outer disk and make the galaxy look younger (Kamphuis & Briggs 1992).

The age and dust extinction maps of M101 show that the central region is younger, more active in star formation, and more dusty. While in the surrounding regions ($r = 20''$), the stellar populations are dominated by old bulge stars and relatively dust-free. These old stellar populations are similar to those of typical bulges or early-type galaxies, which are expected to be less attenuated than star-forming galaxies (Calzetti 2001).

In our results, we find that M 101 has a radial tendency of the star formation time scale, which is shorter in the center and longer outside. Actually, the typical timescale in the form of the exponentially declining SFH of an elliptical galaxy is about 1 Gyr, those of S0 and Sa–Sd spiral galaxies range from 2 to 30 Gyr, and the star formation rate of an irregular galaxy is constant (Bolzonella et al. 2000). Note that for a given stellar population, the Sandage SFH gives a much shorter timescale than the normal exponential SFH. Inner parts of the galaxy, such as the bulge, resemble early-type elliptical galaxies. Most stars in these areas formed in the very early time, implying a short timescale. The outer disk is undergoing a continuous star formation, like late-type spiral or irregular galaxies, giving the longer timescale. Compared with the assumption of a single star formation law (i.e., a single timescale) overall the galaxy, a variational timescale should be more suitable for realistic galaxies. At the same time, this kind of timescale distribution might be important in future studies of stellar populations in different regions of galaxies and in simulations of the galactic evolution.

There are radial metallicity gradients both in the stellar content and gas-rich H II regions. The gradient of the stellar abundance is flatter and the gas-phase gradient is much steeper. In fact, many observations of nearby spiral galaxies show that the inner disk has higher metallicity than the outer disk and the typical gradient of H II regions is about $-0.05 \text{ dex kpc}^{-1}$ (Pilkington et al. 2012). The gas-phase metallicity gradient of M 101 is about $-0.045 \text{ dex kpc}^{-1}$, which is lower than the average gradient of other Sc or Scd type galaxies, such as M33, NGC 2403, and NGC 3184 (Zaritsky et al. 1994). There is some evidence showing that interacting pairs might have systematically lower metallicities than field galaxies (Kewley et al. 2006) and recent mergers also make the metallicity gradient flatten. M 101 is the main body in the M 101 group. It might be interacting with NGC 5474 and NGC 5477 in the group as suggested by Mihos et al. (2012a,b), who declared, with the deep neutral hydrogen observation and deep optical images, that the group is in a dynamically active state and encounters in the group environment are building up the outer disk of M 101. In a whole,

the existence of a metallicity gradient in M 101 supports an inside-out disk growth scenario: the early gas infall or collapse made the small inner region more metal-rich and the outer disk was enriched more slowly (Wang et al. 2011).

From the metallicity map in Figure 9, we also notice that the abundance in the inter-arm regions is poorer than spiral arms. It was expected by some numerical models that establish density waves to trigger star formation. Roy & Kunth (1995) suggested that some azimuthal mixing processes such as super-shell expansion are able to wipe out the abundance inhomogeneities of the interstellar medium in a few galactic rotation (maybe about 1–3 Gyr).

7.2. Bar-induced Secular Evolution

At early times, the galactic evolution was leaded by a combination of dissipative collapses and mergers. The evolution timescale was short and the processes were violent (Toomre 1977; Sandage 1990). In the local universe, some internal secular processes become dominant. These secular processes tend to make late-type galaxies to be bulgeless or have pseudobulge (Kormendy & Kennicutt 2004).

Kormendy et al. (2010) have used the Hobby-Eberly Telescope to obtain high-resolution spectra of nuclear star clusters in M 101 and NGC 6946. They found that the nucleus of M101 has an average rotation velocity of about $210 \pm 15 \text{ km s}^{-1}$, but the velocity dispersion is only about $25 \pm 7 \text{ km s}^{-1}$. Fisher & Drory (2010) measured the $3.6 - 8.0 \mu\text{m}$ color as a rough estimate of the specific star formation rate and reported that the bulge of M 101 is mildly active. The Sérsic index of the bulge is about 1.8 (Fisher et al. 2009), which is less than 2. The central region of M 101 is younger than the surrounding inner disk as shown in our age map, indicating that there is recent star forming in the bulge. The above characteristics, including kinematics dominated by rotation, small velocity dispersion, nearly exponential brightness profile ($n_b < 2$), and relatively active star formation, show that the bulge of M 101 is a so-called pseudobulge, which reserves some features of the disk.

The pseudobulge is believed to form via the internal secular evolution of the disk (Kormendy & Kennicutt 2004; Fisher et al. 2009). The nonaxisymmetries of the gravitational potentials from bars, ovals, and/or spiral arms would rearrange the mass and angular momentum and cause gas infall to build up the central mass concentration. In normal spiral galaxies without bars and ovals, shocks actuated by the density wave make gas in the disk lose energy and drop into the center, which gradually forms the disk-like bulge. For barred galaxy, gravitational torques and shocks cause the gas inflow along the bar ends to trigger star formation and make young stellar populations and central mass convergence. For more

information about the secular evolution and pseudobulges, refer to the review of Kormendy & Kennicutt (2004).

The CO radio observations show that there is a bar-like morphology in the center of M 101 (Kenney et al. 1991). The bar feature has a length of $1'.5 \pm 0'.5$ with a position angle of $102^\circ \pm 4^\circ$. This feature is expected to appear at the inner Lindblad resonances (ILR). The gas in the disk is likely to stream along the molecular bar, pile up at the ILRs, and trigger star formation (Athanasoula 1992; Roming et al. 1999). From the maps of age, metallicity, dust extinction, and the optical image from the Hubble Space Telescope (HST), a bar-like knot in the center can be resolved, which is relatively young, metal-rich, and dusty. In addition, the parameter discrepancies between the pseudobulge and inner parts of the disk are larger in the maps than in the radial profiles which might be smoothed by the bar feature. Thus, evolutions of the pseudobulge and disk is probably ruled by some secular processes of the gas-rich bar. Among late-type spirals including M 101, the average length of bars is small, indicating a slow process of gas accretion (Sheth 2001). The star formation is also slower than early-type barred spiral galaxies (Martin & Kennicutt 2001). Thus, such kind of secular process is less obvious in late-type spiral galaxies.

8. SUMMARY

Radial gradients of stellar population properties have imprints of the galactic formation and evolution. Colors and spectral lines are usually used to investigate the stellar population and chemical abundance of galaxies, but there are serious degeneracy effects of age, metallicity, and dust attenuation. Multi-band photometric data from ultraviolet, optical, and infrared observations can help us to degrade this kind of degeneracy. By fitting with the evolutionary stellar population synthesis models, we have derived spatially resolved distributions of age, metallicity, dust extinction, and star formation timescale in a nearby Scd galaxy M 101. In our fitting method, we constrain the dust attenuation with the $\text{IRX-}A_{\text{FUV}}$ relation, which is found to strongly correlate to a second parameter of birth rate b . This parameter is related to both age and star formation history.

From the results, we find that there are clear gradients of different parameters, supporting the so-called “inside-out” disk growth scenario. Some conclusions are presented as follows:

- 1) The stellar disk is optically thicker in the inner region than the outer region. The overall dust extinction of M 101 is measured to be about 0.24 mag, which is a little lower than galaxies of similar morphological type and much lower than those of earlier type. The

core of this galaxy is somewhat dusty. Extinctions of H II regions from both our MMT observations and literatures also show the same radial tendency. The dust attenuation of the stellar content is much lower than that of H II regions, and a rough linear correlation is obtained as $A_V^{\text{star}} = 0.32A_V^{\text{neb}} + 0.06$.

2) The stellar metallicity has a gradient of $-0.011 \text{ dec kpc}^{-1}$, lower than that of the gas-phase abundance gradient ($-0.045 \text{ dec kpc}^{-1}$) derived by the spectra of H II regions from MMT observations and literatures. The metallicity gradient of M 101 is flatter than those of Sc and Scd type galaxies, because interactions and mergers might lower the metallicity and make it flatten, which was suggested by Kewley et al. (2006). Actually, M 101 is located in a small group, and it might be interacting with two other members NGC 5474 and NGC 5477 as indicated in Mihos et al. (2012a,b).

3) Two distinct regions of the stellar disk with different age and color gradients are discovered. The age gradient of the inner region is steeper and that of the outer region is flatter, which might be caused by the secular dynamical evolution of the disk.

4) We highlight that a variational star formation timescale should more exactly describe a real galaxy than just a single timescale in the form of SFH. The timescale of M 101 increases gradually from the galactic center to outskirts. It should be reasonable, because the bulge in the center resembles elliptical galaxies with small typical timescales and the outer region of the disk is similar to late-type spirals with large timescales.

5) The bulge of M 101 is younger, more dusty, and more metal-rich than surrounding inner disk regions, indicating that it has been forming stars recently. Active star formation in this galaxy, together with other observations including high rotation velocity, low velocity dispersion, and nearly exponential brightness profile, indicates that the bulge is a so-called pseudobulge. From our age, metallicity, and dust maps as well as gas distribution from radio observations, we find that there is a resolved bar in the center. Thus, the growth of the pseudobulge and evolution of the disk are likely to be induced by some secular processes of the bar, whose gravitational potential causes the gas to fall through the bar ends, triggers star formation, and makes central mass concentration.

We thank the referee for his/her thoughtful comments and insightful suggestions that improve our paper greatly. This work is based in part on observations made with the Spitzer Space Telescope, which is operated by the Jet Propulsion Laboratory, California Institute of Technology under a contract with NASA. This publication makes use of data products from the Two Micron All Sky Survey, which is a joint project of the University of Massachusetts and the Infrared Processing and Analysis Center/California Institute of Technology, funded by the National Aeronautics and Space Administration and the National Science Foundation.

This research also use data obtained through the Telescope Access Program (TAP), which is funded by the National Astronomical Observatories of China and the Special Fund for Astronomy from the Ministry of Finance. This work is supported by the National Natural Science Foundation of China (NSFC, Nos. 11073032, 11203031, and 11225315) and Chinese Universities Scientific Fund (CUSF) and Specialized Research Fund for the Doctoral Program of Higher Education (SRFDP, No. 20123402110037).

REFERENCES

- Athanassoula, E. 1992, *MNRAS*, 259, 345
- Bakos, J., Trujillo, I., & Pohlen, M. 2008, *ApJ*, 683, L103
- Bertin, E. 2011, *Astronomical Data Analysis Software and Systems XX*, 442, 435
- Bertin, E., & Arnouts, S. 1996, *A&AS*, 117, 393
- Bianchi, L., Thilker, D. A., Burgarella, D., et al. 2005, *ApJ*, 619, L71
- Boissier, S., Boselli, A., Buat, V., Donas, J., & Milliard, B. 2004, *A&A*, 424, 465
- Bolzonella, M., Miralles, J.-M., & Pelló, R. 2000, *A&A*, 363, 476
- Boselli, A., Gavazzi, G., & Sanvito, G. 2003, *A&A*, 402, 37
- Bosma, A., Goss, W. M., & Allen, R. J. 1981, *A&A*, 93, 106
- Bresolin, F. 2007, *ApJ*, 656, 186
- Bruzual, G., & Charlot, S. 2003, *MNRAS*, 344, 1000
- Buat, V. 1992, *A&A*, 264, 444
- Calzetti, D. 2001, *PASP*, 113, 1449
- Calzetti, D., Kennicutt, R. C., Jr., Bianchi, L., et al. 2005, *ApJ*, 633, 871
- Cameron, E., Driver, S. P., Graham, A. W., & Liske, J. 2009, *ApJ*, 699, 105
- Carollo, C. M., Scarlata, C., Stiavelli, M., Wyse, R. F. G., & Mayer, L. 2007, *ApJ*, 658, 960
- Chabrier, G. 2003, *PASP*, 115, 763
- Cortese, L., Boselli, A., Franzetti, P., et al. 2008, *MNRAS*, 386, 1157

- da Cunha, E., Charlot, S., & Elbaz, D. 2008, MNRAS, 388, 1595
- Daddi, E., Renzini, A., Pirzkal, N., et al. 2005, ApJ, 626, 680
- Fan, X., Burstein, D., Chen, J.-S., et al. 1996, AJ, 112, 628
- Fisher, D. B., & Drory, N. 2010, ApJ, 716, 942
- Fisher, D. B., Drory, N., & Fabricius, M. H. 2009, ApJ, 697, 630
- Fitzpatrick, E. L. 1986, AJ, 92, 1068
- Ganda, K., Peletier, R. F., McDermid, R. M., et al. 2007, MNRAS, 380, 506
- Gavazzi, G., Bonfanti, C., Sanvito, G., Boselli, A., & Scodeggio, M. 2002, ApJ, 576, 135
- Grevesse, N., & Sauval, A. J. 1998, Space Sci. Rev., 85, 161
- Groves, B., Dopita, M. A., Sutherland, R. S., et al. 2008, ApJS, 176, 438
- Hao, C.-N., Kennicutt, R. C., Johnson, B. D., et al. 2011, ApJ, 741, 124
- Jarrett, T. H., Chester, T., Cutri, R., Schneider, S. E., & Huchra, J. P. 2003, AJ, 125, 525
- Kamphuis, J., & Briggs, F. 1992, A&A, 253, 335
- Kauffmann, G., Heckman, T. M., White, S. D. M., et al. 2003, MNRAS, 341, 33
- Kenney, J. D. P., Scoville, N. Z., & Wilson, C. D. 1991, ApJ, 366, 432
- Kennicutt, R. C., Jr., Bresolin, F., & Garnett, D. R. 2003, ApJ, 591, 801
- Kennicutt, R. C., Jr., Calzetti, D., Walter, F., et al. 2007, ApJ, 671, 333
- Kennicutt, R. C., Jr., & Garnett, D. R. 1996, ApJ, 456, 504
- Kennicutt, R. C., Jr., Hao, C.-N., Calzetti, D., et al. 2009, ApJ, 703, 1672
- Kewley, L. J., Geller, M. J., & Barton, E. J. 2006, AJ, 131, 2004
- Kobulnicky, H. A., & Kewley, L. J. 2004, ApJ, 617, 240
- Kong, X., Zhou, X., Chen, J., et al. 2000, AJ, 119, 2745
- Kong, X., Charlot, S., Brinchmann, J., & Fall, S. M. 2004, MNRAS, 349, 769
- Kormendy, J., Drory, N., Bender, R., & Cornell, M. E. 2010, ApJ, 723, 54

- Kormendy, J., & Kennicutt, R. C., Jr. 2004, *ARA&A*, 42, 603
- Kroupa, P. 2002, *Science*, 295, 82
- Kuntz, K. D., Harrus, I., McGlynn, T. A., Mushotzky, R. F., & Snowden, S. L. 2008, *PASP*, 120, 740
- Lee, J. C., Kennicutt, R. C., Engelbracht, C. W., et al. 2008, *Formation and Evolution of Galaxy Disks*, 396, 151
- Li, J.-L., Zhou, X., Ma, J., & Chen, J.-S. 2004, *Chinese J. Astron. Astrophys.*, 4, 143
- MacArthur, L. A., Courteau, S., Bell, E., & Holtzman, J. A. 2004, *ApJS*, 152, 175
- MacArthur, L. A., González, J. J., & Courteau, S. 2009, *MNRAS*, 395, 28
- Ma, J., de Grijs, R., Fan, Z., et al. 2009, *Research in Astronomy and Astrophysics*, 9, 641
- Martin, C. L., & Kennicutt, R. C., Jr. 2001, *ApJ*, 555, 301
- Martin, D. C., Fanson, J., Schiminovich, D., et al. 2005, *ApJ*, 619, L1
- McCall, M. L., Rybski, P. M., & Shields, G. A. 1985, *ApJS*, 57, 1
- Meurer, G. R., Heckman, T. M., & Calzetti, D. 1999, *ApJ*, 521, 64
- Mihos, C., Harding, P., Spengler, C., Rudick, C., & Feldmeier, J. 2012a, *arXiv:1211.3095*
- Mihos, C., Keating, K., Holley-Bockelmann, K., Pisano, D. J., & Kassim, N. 2012b, *arXiv:1210.8333*
- Mao, Y.-W., Kennicutt, R. C., Jr., Hao, C.-N., Kong, X., & Zhou, X. 2012, *ApJ*, 757, 52
- Muñoz-Mateos, J. C., Gil de Paz, A., Boissier, S., et al. 2009, *ApJ*, 701, 1965
- Noll, S., Burgarella, D., Giovannoli, E., et al. 2009, *A&A*, 507, 1793
- Pahre, M. A., Ashby, M. L. N., Fazio, G. G., & Willner, S. P. 2004, *ApJS*, 154, 229
- Peletier, R. F., Davies, R. L., Illingworth, G. D., Davis, L. E., & Cawson, M. 1990, *AJ*, 100, 1091
- Pierini, D., Gordon, K. D., Witt, A. N., & Madsen, G. J. 2004, *ApJ*, 617, 1022
- Pilkington, K., Few, C. G., Gibson, B. K., et al. 2012, *A&A*, 540, A56

- Roškar, R., Debattista, V. P., Stinson, G. S., et al. 2008, *ApJ*, 675, L65
- Roming, P. W. A., Moody, J. W., & Hintz, E. G. 1999, *AJ*, 117, 1733
- Rosa, M. R., & Benvenuti, P. 1994, *A&A*, 291, 1
- Roy, J.-R., & Kunth, D. 1995, *A&A*, 294, 432
- Salim, S., Rich, R. M., Charlot, S., et al. 2007, *ApJS*, 173, 267
- Salpeter, E. E. 1955, *ApJ*, 121, 161
- Sánchez-Blázquez, P., Courty, S., Gibson, B. K., & Brook, C. B. 2009, *MNRAS*, 398, 591
- Sandage, A. 1990, *JRASC*, 84, 70
- Scalo, J. M., & Struck-Marcell, C. 1986, *ApJ*, 301, 77
- Schlegel, D. J., Finkbeiner, D. P., & Davis, M. 1998, *ApJ*, 500, 525
- Sheth, K. 2001, *The Central Kiloparsec of Starbursts and AGN: The La Palma Connection*, 249, 605
- Silva, L., Granato, G. L., Bressan, A., & Danese, L. 1998, *ApJ*, 509, 103
- Skrutskie, M. F., Cutri, R. M., Stiening, R., et al. 2006, *AJ*, 131, 1163
- Tamura, N., & Ohta, K. 2003, *AJ*, 126, 596
- Tinsley, B. M. 1972, *A&A*, 20, 383
- Toomre, A. 1977, *Evolution of Galaxies and Stellar Populations*, 401
- Trujillo, I., Förster Schreiber, N. M., Rudnick, G., et al. 2006, *ApJ*, 650, 18
- van Zee, L., Salzer, J. J., Haynes, M. P., O’Donoghue, A. A., & Balonek, T. J. 1998, *AJ*, 116, 2805
- Vazdekis, A. 1999, *ApJ*, 513, 224
- Wang, J., Kauffmann, G., Overzier, R., et al. 2011, *MNRAS*, 412, 1081
- Williams, B. F., Dalcanton, J. J., Dolphin, A. E., Holtzman, J., & Sarajedini, A. 2009, *ApJ*, 695, L15
- Worthey, G. 1994, *ApJS*, 95, 107

- Wyse, R. F. G., Gilmore, G., Norris, J. E., et al. 2006, ApJ, 639, L13
- Zaritsky, D., Kennicutt, R. C., Jr., & Huchra, J. P. 1994, ApJ, 420, 87
- Zibetti, S., Charlot, S., & Rix, H.-W. 2009, MNRAS, 400, 1181
- Zou, H. 2011a, PASP, 123, 1135
- Zou, H., Yang, Y.-B., Zhang, T.-M., et al. 2011b, Research in Astronomy and Astrophysics, 11, 1093
- Zou, H., Zhang, W., Yang, Y., et al. 2011c, AJ, 142, 16

Table 1. FIFTEEN BATC FILTERS AND STATISTICS OF OBSERVATIONS

No.	Name ^a	λ_{eff} ^b	Exp. Time ^c	FWHM ^d
1	a	3360	10800	4.38
2	b	3890	14400	3.85
3	c	4210	6000	4.30
4	d	4550	18000	5.20
5	e	4920	12000	3.98
6	f	5270	10800	3.88
7	g	5795	7200	3.83
8	h	6075	3600	5.38
9	i	6660	7200	3.90
10	j	7050	7200	4.18
11	k	7490	7200	4.29
12	m	8020	8400	4.85
13	n	8480	6000	3.73
14	o	9190	10800	4.09
15	p	9745	12000	4.56

^aLetters denote the filters in the BATC photometric system.

^bEffective wavelengths in Å.

^cTotal exposure times in seconds.

^dFWHMs of the stacked images in arcsec.

Table 2. STANDARD DEVIATIONS OF PARAMETERS DERIVED BY FITTING
SIMULATED SEDS IN DIFFERENT S/NS

S/N	$\sigma(\log t)$	$\sigma(\log Z)$	$\sigma(\tau)$	$\sigma(b)$	$\sigma(A_V)$
5	0.16	0.17	1.23	0.24	0.13
10	0.13	0.10	1.24	0.19	0.07
20	0.11	0.06	1.27	0.16	0.05

Note. — The units are yr for age t , mag for A_V , and dex for logarithmic quantities.

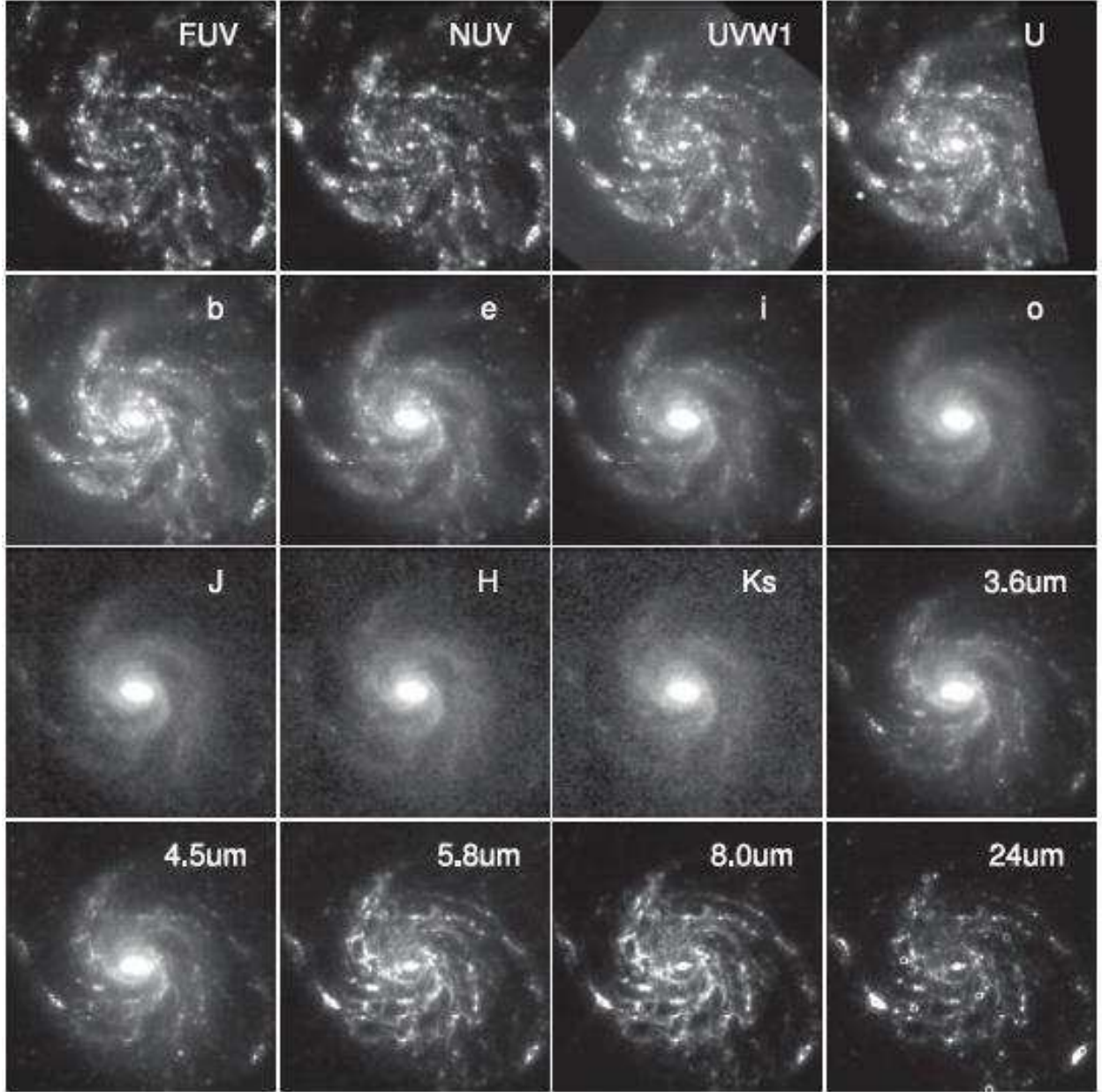


Fig. 1.— Multi-band morphologies of M101. The image size is about $20' \times 20'$, corresponding to 43×43 kpc at the distance of 7.4 Mpc. All the images are shown with the same spatial scale of $1.7''$. North is up and east is left.

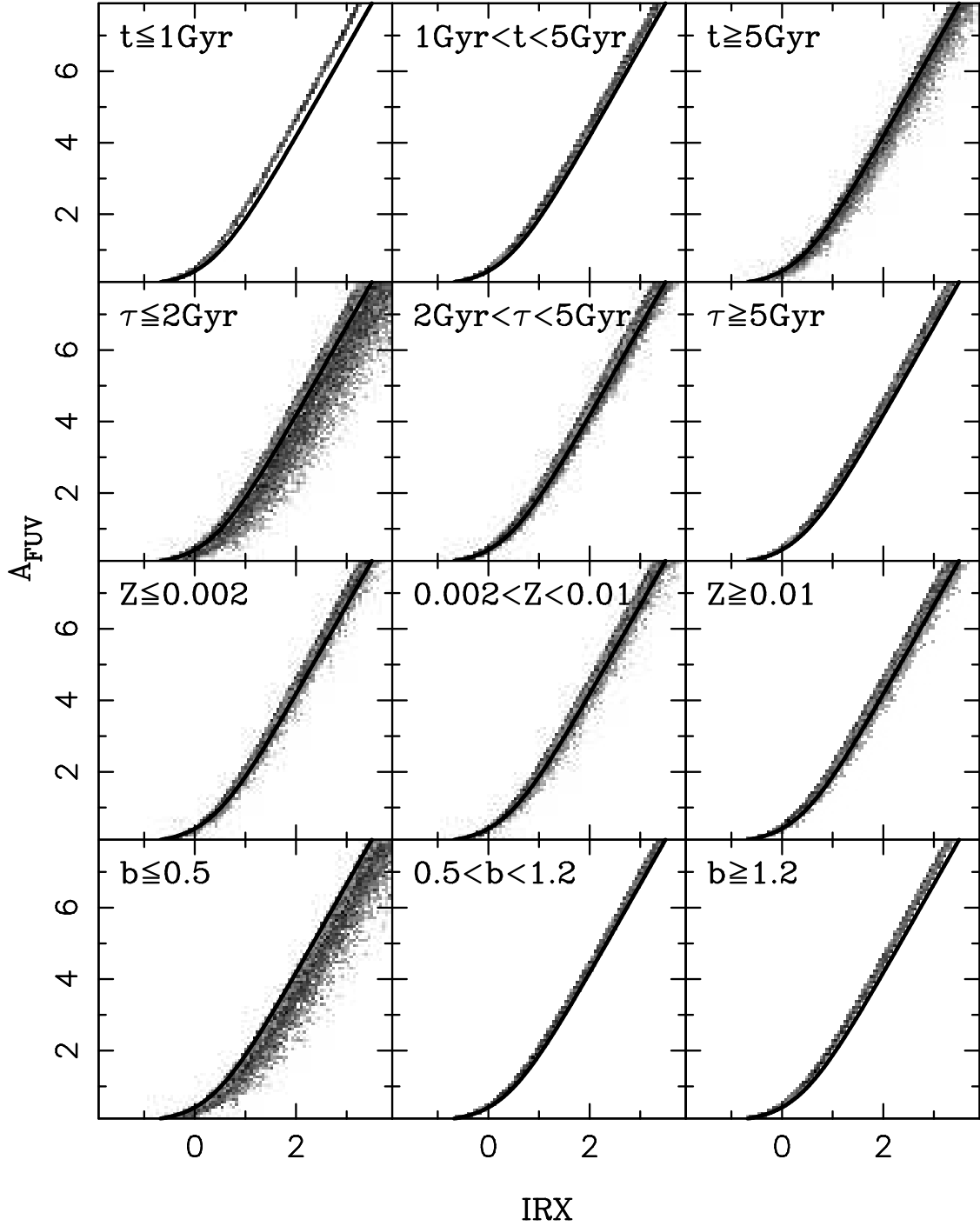


Fig. 2.— Relationship between IRX and A_{FUV} within different ranges of parameters. From top to bottom, this relation is plotted in different bins of age t , star formation timescale τ , metallicity Z , and birth rate b . The IRX- A_{FUV} relation calibrated by Hao et al. (2011) is also overlapped in solid lines.

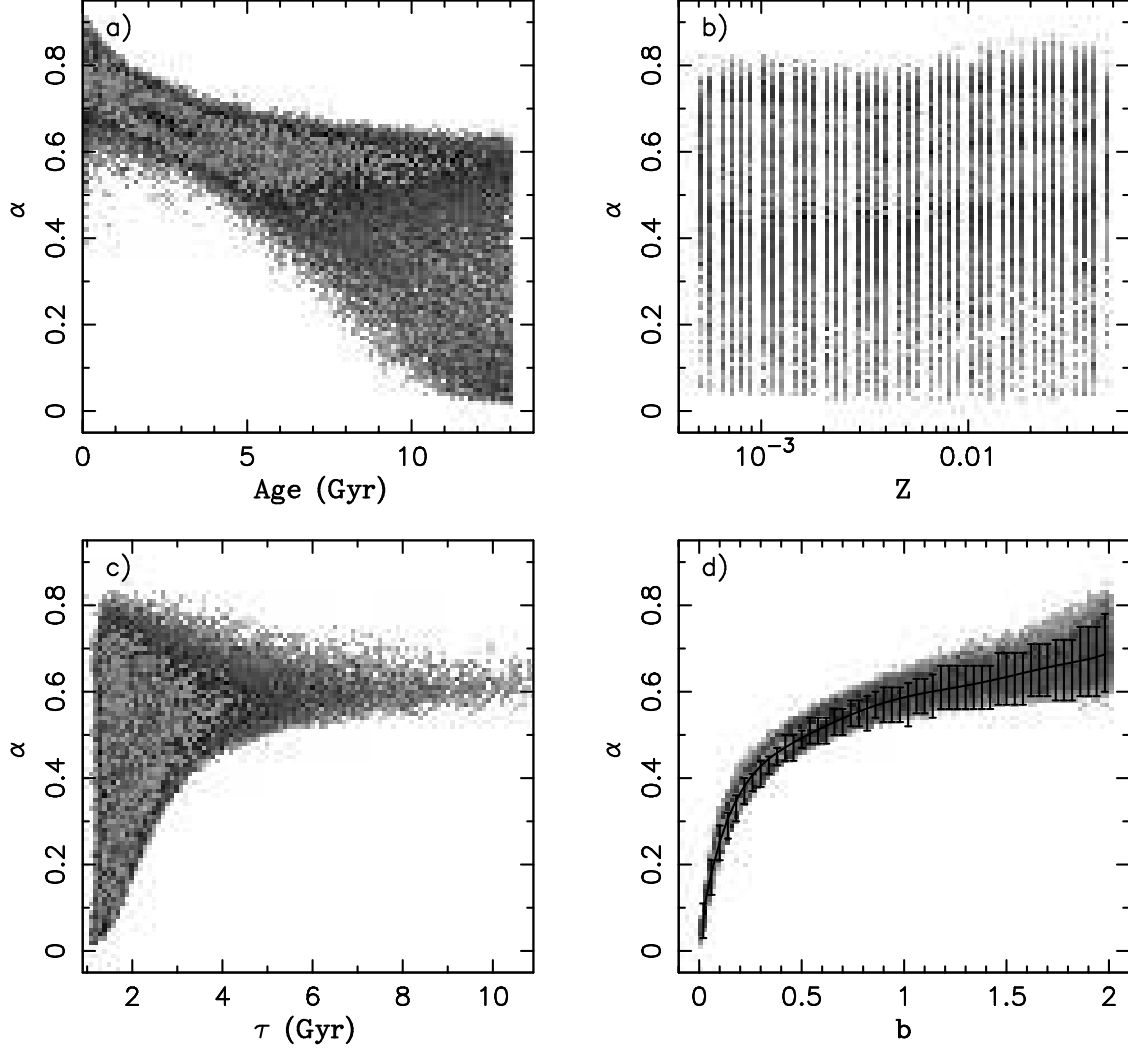


Fig. 3.— Scale factor α in Equation (1) as functions of age (top left), metallicity (top right), star formation timescale (bottom left), and birth rate (bottom right). The solid curve in the bottom right panel is the fitted polynomial as shown in Equation (2) and points with error bars denote means and standard deviations of α values in given bins of b .

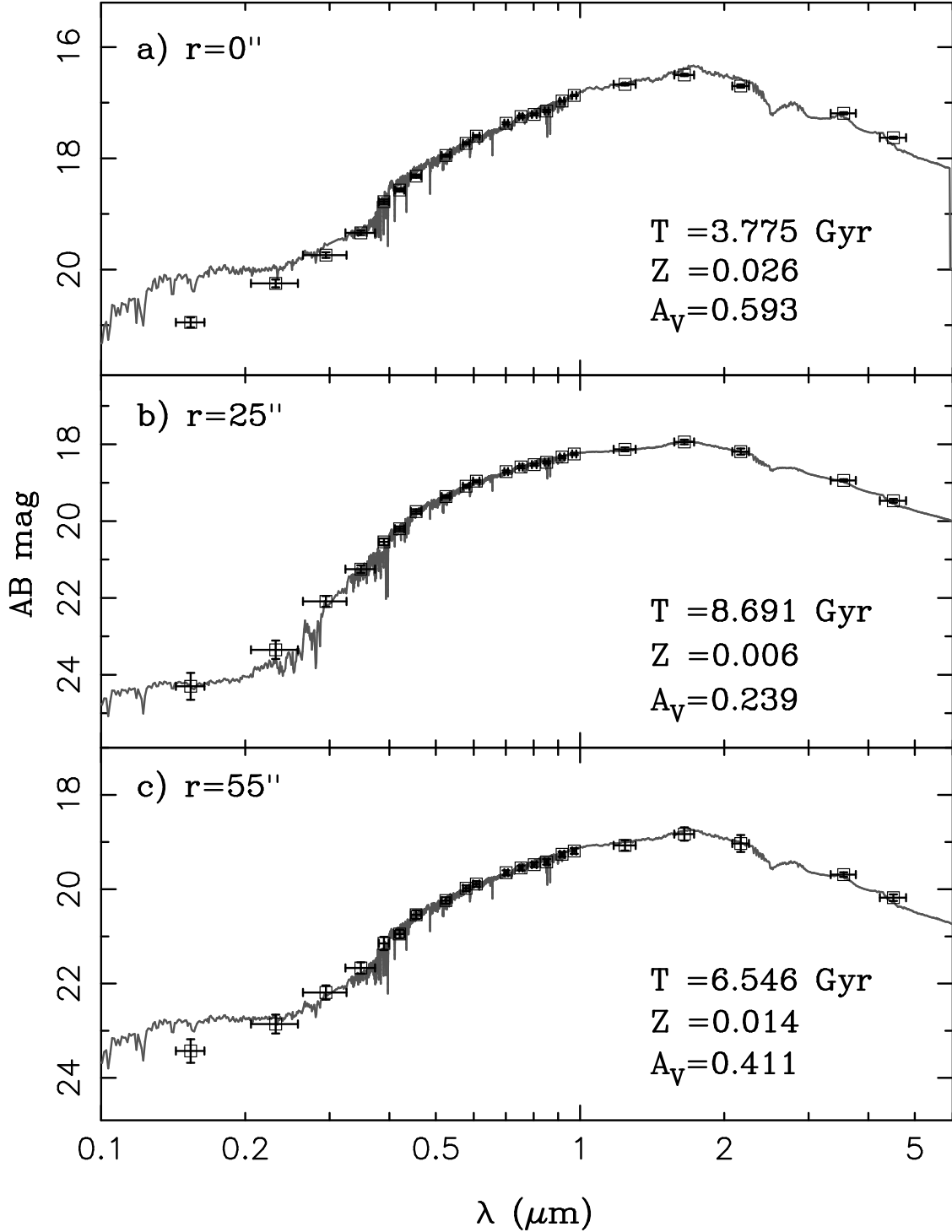


Fig. 4.— Observed SEDs and best fitted model spectra for randomly chosen positions at different galactocentric radii. For each observed SED in open rectangles, the vertical bars indicate the photometric errors, while the horizontal bars show the effective bandwidths of the photometric bands. The model spectra are plotted in grey lines. Best fitted values of age, metallicity, extinction are also shown in each panel.

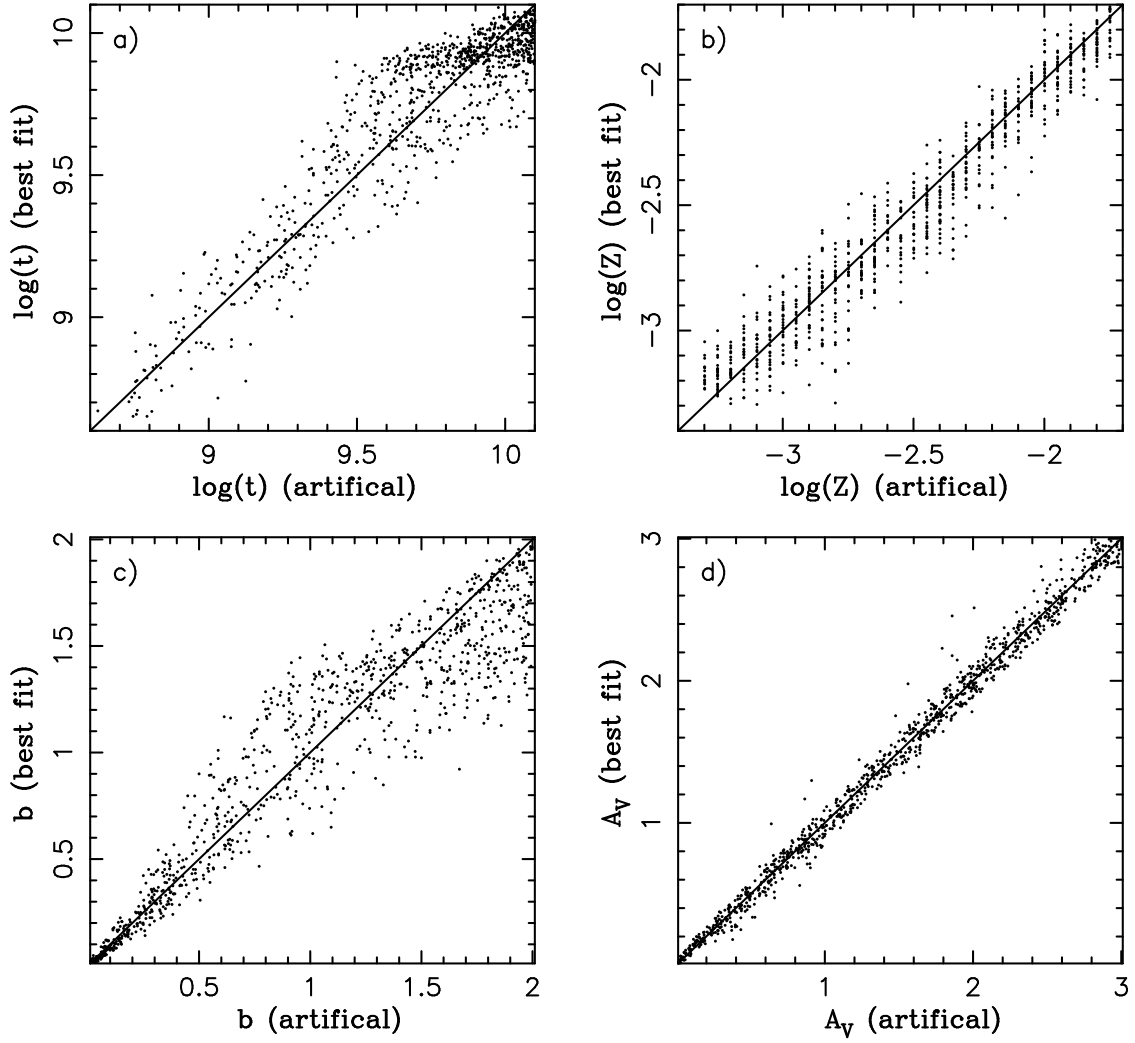


Fig. 5.— Comparisons between the best-fitted and input parameters after fitting the simulated SEDs (S/N of 10) with the models. The units are yr for age, mag for A_V , and dex for logarithmic quantities. Diagonal lines mean that the input parameters are equal to the fitted output parameters.

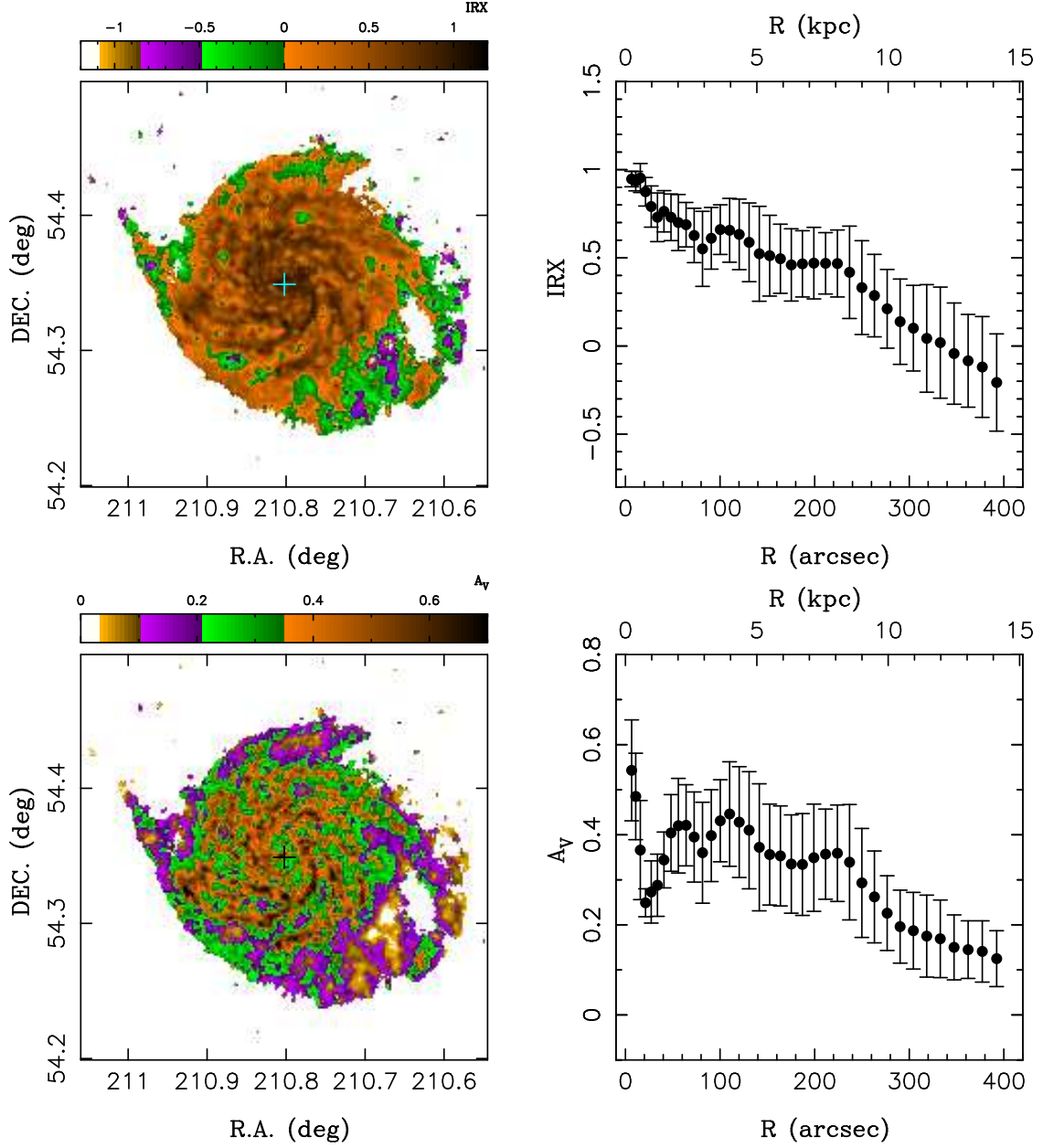


Fig. 6.— IRX and A_V maps and their corresponding radial profiles. The cross is the optical center of M 101. Error bars in all the radial profiles of this paper are standard deviations of parameter values in given annuli.

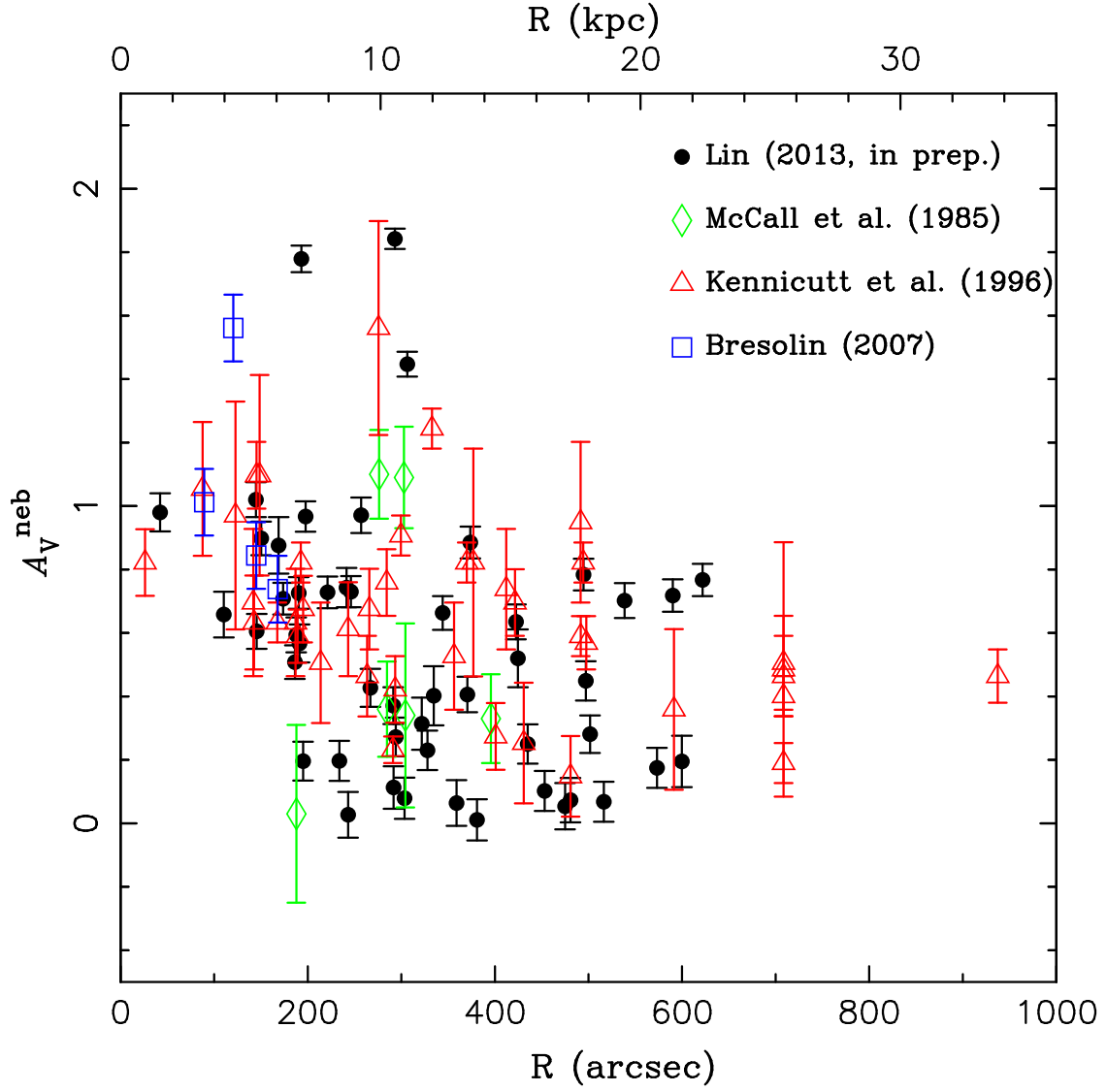


Fig. 7.— Gas-phase attenuation A_V^{neb} derived from H II regions. The points drawn in different symbols come from different literatures.

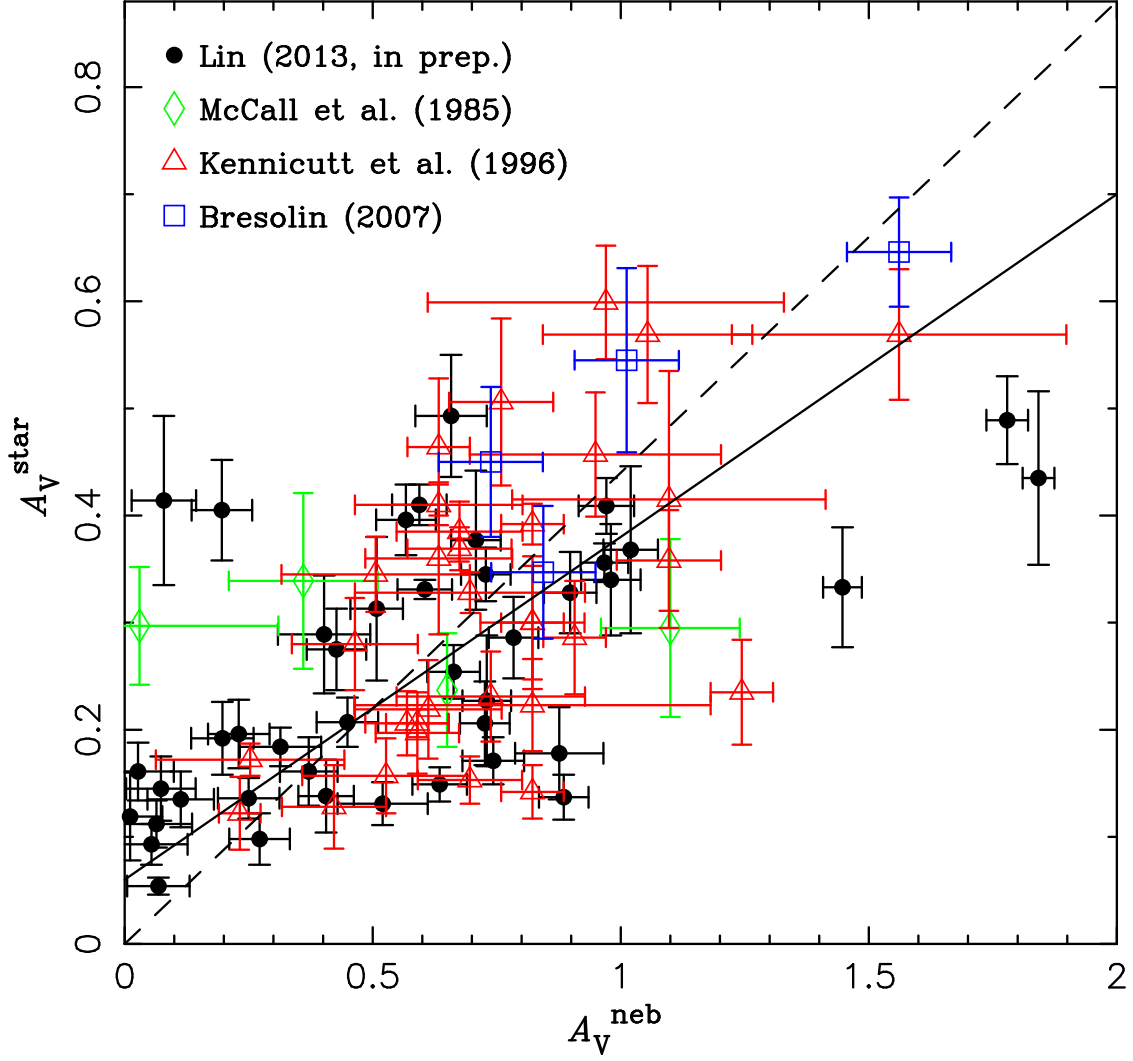


Fig. 8.— Comparison of A_V from both stellar measurements and nebular emissions in M101. The dashed line shows the relation from Calzetti (2001): $A_V^{\text{star}} = 0.44 A_V^{\text{neb}}$. The solid line displays the linear fitting to our data, which gives a flatter relation: $A_V^{\text{star}} = 0.32 A_V^{\text{neb}} + 0.06$.

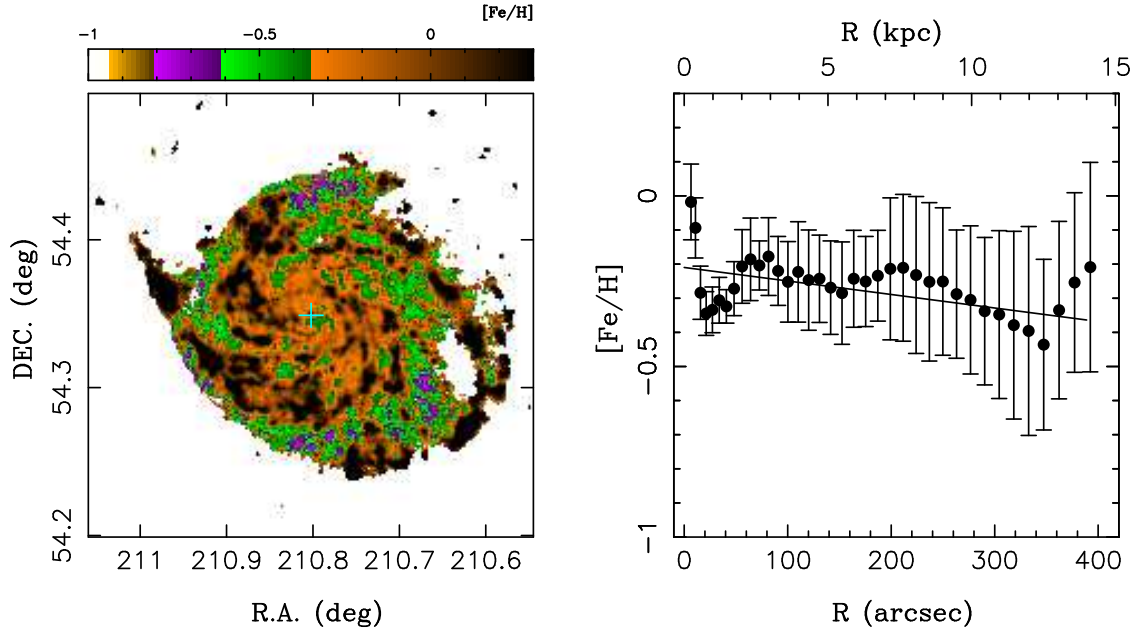


Fig. 9.— Metallicity map in $[\text{Fe}/\text{H}]$ and its radial profile of M 101. The cross is the optical center of M 101. The line in the radial profile gives the linearly fitted gradient of about $-0.011 \text{ dex kpc}^{-1}$.

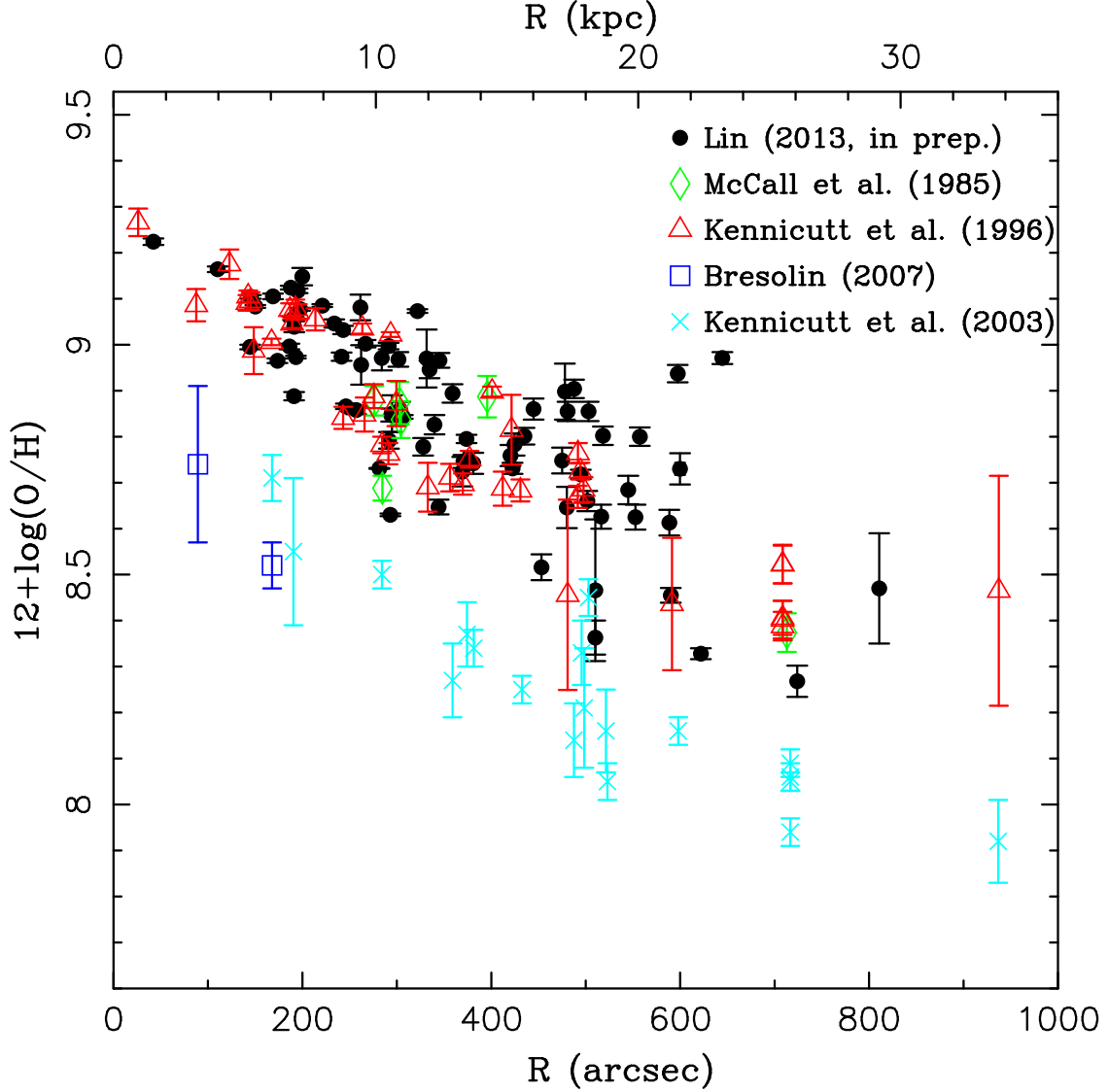


Fig. 10.— Oxygen abundance as a function of the deprojected galactocentric distance for individual H II regions in M 101. Different symbols denote the data from different literatures. Dark circles and orange triangles correspond to oxygen abundances computed by the KK04 calibration (Kobulnicky & Kewley 2004). Green crosses and blue squares represent oxygen abundances derived by the T_e method. The KK04 calibration yields abundances that are 0.5 dex higher than those based on the T_e method, but the abundance gradients are consistent based on different calibrations.

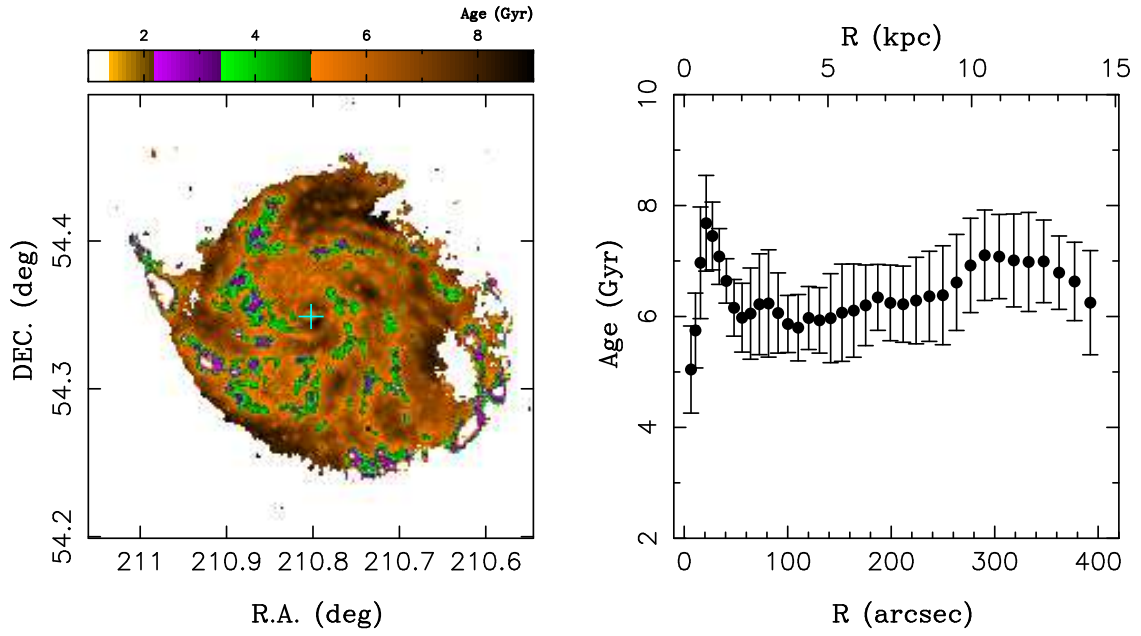


Fig. 11.— Age map and its radial profile. The cross is the optical center of M 101.

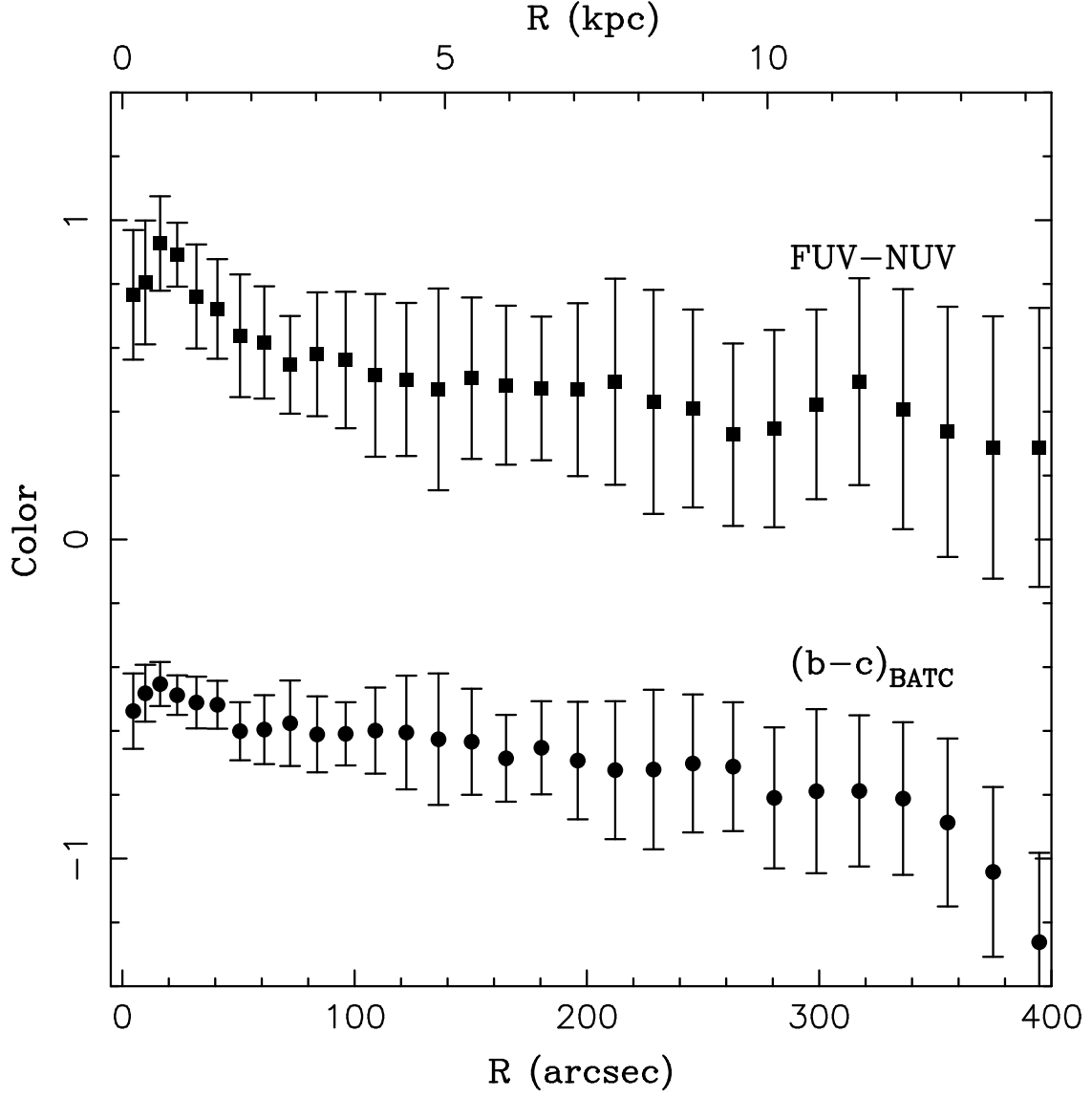


Fig. 12.— Radial profiles of the $FUV-NUV$ and BATC $b-c$ colors. The $b-c$ color is shifted by an arbitrary value.

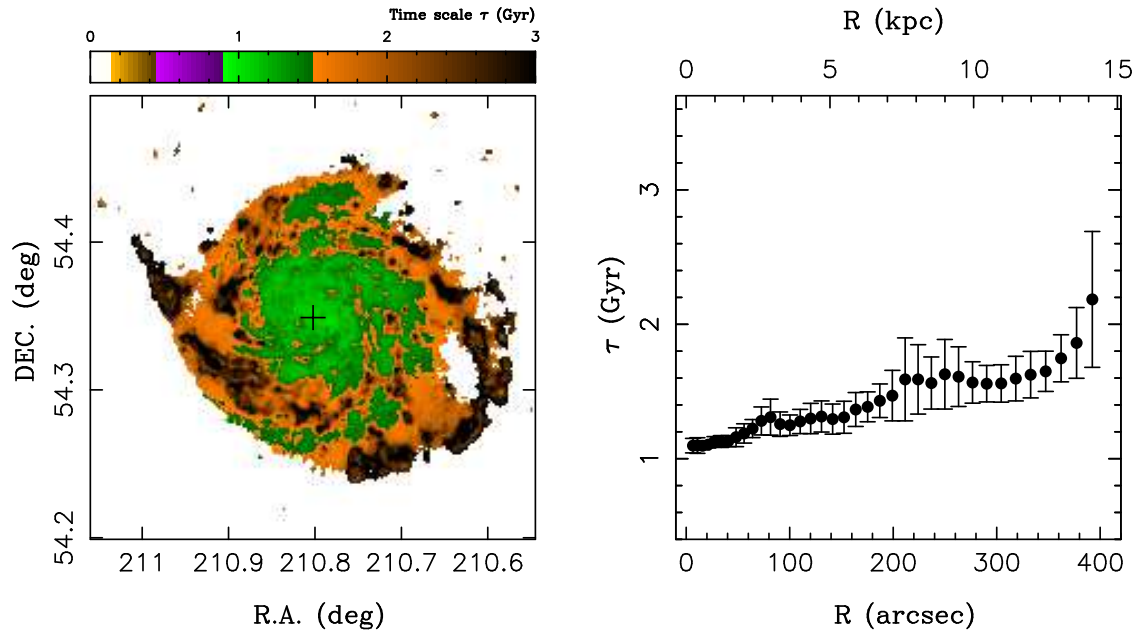


Fig. 13.— Map of star formation time scale and its radial profile. The cross is the optical center of M 101.